ACS NANOSCIENCE Au
AN OPEN ACCESS JOURNAL OF THE AMERICAN CHEMICAL SOCIETY

pubs.acs.org/nanoau Article

Superatomic $Au_{25}(SC_2H_5)_{18}$ Nanocluster under Pressure

Qing Tang, Fuhua Li, and De-en Jiang*

Cite This: ACS Nanosci. Au 2022, 2, 40−48

Read Online

ACCESS | Metrics & More | Article Recommendations | Supporting Information

ABSTRACT: The past decade has witnessed significant advances in the synthesis and structure determination of atomically precise metal nanoclusters. However, little is known about the condensed matter properties of these nanosized metal nanoclusters packed in a crystal lattice under high pressure. Here using density functional theory calculations, we simulate the crystal of a representative superatomic gold cluster, $Au_{25}(SR)_{18}{}^{0}$ (R = C_2H_5), under various pressures. At ambient conditions, $Au_{25}(SC_2H_5)_{18}{}^{0}$ clusters are packed in a crystal via dispersion interactions; being a 7e superatom, each cluster carries a magnetic moment of 1 μ_B or one unpaired electron. Upon increasing compression (from 10 to 110 GPa), we observe the formation of intercluster Au−Au, Au−S, and S−S covalent bonds between staple motifs, thereby linking the clusters into a network. The pressure-induced structural change is accompanied by the vanishment of the magnetic moment and the semiconductor-to-metal transition. Our work shows that subjecting crystals of atomically precise metal nanoclusters to high pressures could lead to new crystalline states and physical properties.

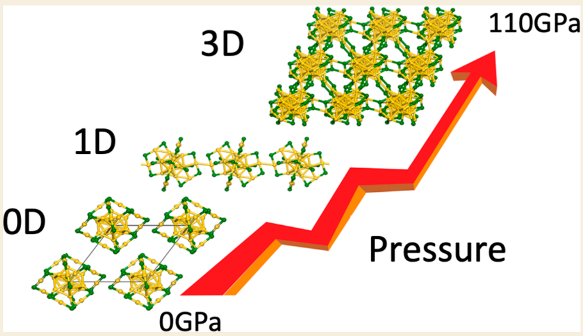

KEYWORDS: *superatoms, ligand-protected gold nanoclusters, crystal structure, high pressure, density functional theory, cluster−cluster interactions*

INTRODUCTION

High-pressure studies have enriched the structural chemistry of compounds and led to unusual properties such as high (room)-temperature superconductivity,[1,2] metal-to-semiconductor transition,[3] and superfluidity.[4] In recent years, researchers have subjected many hydrogen-containing substances (H_2,[4] SiH_4,[5] H_2S,[1,6] etc.) and other inorganic systems (He,[7] Li,[3,8,9] LiN_3,[10] Si,[11] SiO,[12] SiO_2,[13] etc.) to high pressures, finding intriguing chemical and physical properties.[14,15]

In the past decade, the ligand-protected metal nanoclusters, especially the thiolated gold nanoclusters, have attracted great interest as a novel type of functional nanomaterials.[16−19] Due to their interesting structural and physicochemical properties, these nanoclusters can be potentially applied in diverse fields, including catalysis,[20−23] biosensing,[24−27] drug delivery,[28,29] luminescence,[30,31] and molecular electronics.[32−34] Researchers were also interested in the mechanical response of the crystal of atomically precise nanoclusters.[35] However, only a couple of experimental studies have explored their high-pressure properties. Li et al.[36] reported the first high-pressure optical study of a series of face-centered cubic and bitetrahedral nanoclusters, including $Au_{21}(SR)_{12}$, $Au_{28}(SR)_{20}$, $Ag_{28}Pt(SR)_{18}$, $Au_{24}(SR)_{20}$, and $Au_{14}Cd(SR)_{12}$. They observed a red shift in the absorption onset with increasing pressure up to ∼12 GPa in all of the studied nanoclusters and an up to 200-fold enhancement in the photoluminescence at pressures around 7 GPa. In another work, Quan et al.[37] probed the pressure response of a silver sulfide cluster crystal ($[Ag_{50}S_7(SC_6H_4F)_{36}(dppp)_6]$) and observed a noticeable decrease of band gap accompanied by visual thermochromism and piezochromism from ambient conditions to 7.5 GPa.

The recent pioneering experimental studies of atomically precise metal nanoclusters under high pressure are expected to draw more attention and efforts to understand how atomically precise metal nanoclusters change their states and properties with pressure. In particular, one is interested in their behavior at even higher pressures such as tens or even hundreds of GPa. Another question is how their electronic structure would evolve with pressure from the superatomic perspective. To address these questions, here we use density functional theory (DFT) calculations to simulate a crystal of superatomic $Au_{25}(SR)_{18}$, the most studied atomically precise metal nanocluster,[38] under pressures up to 110 GPa. We chose the experimental crystal structure of the neutral $Au_{25}(SC_2H_5)_{18}{}^{0}$ cluster as the starting model for DFT simulations, for its short ligand[39] and to avoid complication from counterions.

Received: September 6, 2021
Revised: October 8, 2021
Accepted: October 11, 2021
Published: October 26, 2021

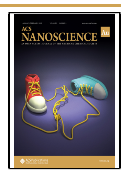

Table 1. Lattice Parameters (a, b, c) of the $Au_{25}(SC_2H_5)_{18}$ Crystal under Various Pressures (Angular Parameters Are Kept at the Same: $\alpha = 104.38°$, $\beta = 101.41°$, $\gamma = 119.29°$)

	lattice parameter (Å)		
pressure (GPa)	*a*	*b*	*c*
0	13.773	13.886	14.152
10	12.395	12.498	12.737
25	11.701	11.798	12.024
50	11.047	11.137	11.350
80	10.715	10.803	11.009
110	10.427	10.514	10.715

Table 2. Covalent and van der Waals Radii of Au, S, C, and H Atoms and Their Averages Which Are Used to Define the Bond Formation between Two Atoms[a]

	radii (Å)			bond-length cutoff (Å)			
atom	covalent	van der Waals	average	Au	S	C	H
Au	1.44	1.66	1.55	3.10	2.96	2.79	2.34
S	1.02	1.80	1.41		2.82	2.65	2.30
C	0.77	1.70	1.24			2.48	2.03
H	0.38	1.20	0.79				1.58

[a]If the distance between two atoms is shorter than the sum of their average radii, we consider that a chemical bond is formed between the two atoms.

■ COMPUTATIONAL METHODS

DFT calculations were performed using the Vienna ab initio simulation package (VASP version 5.4.4).[40] The ion−electron interaction is described with the projector-augmented wave (PAW) method.[41] Electron exchange-correlation is represented by the functional of Perdew, Burke, and Ernzerhof (PBE) of the generalized gradient approximation (GGA).[42] A cutoff energy of 500 eV was used for the plane-wave basis set. The Brillouin zone was sampled by a Monkhorst−Pack *k*-point mesh of 5 × 5 × 5 for geometry optimization and 11 × 11 × 11 for static electronic structure calculation. The convergence threshold for structural optimization was set to be 10^{-5} eV in energy and 0.01 eV/Å in force. The van der Waals (vdW) interactions were considered using the empirical correction in Grimme's scheme (DFT-D3).[43]

The experimental crystal structure of $Au_{25}(SC_2H_5)_{18}^0$ at ambient conditions[39] was used as the initial structure in our DFT model. The crystal has a centrosymmetric triclinic symmetry (space group $P\bar{1}$) with the following parameters: $a = 13.773$ Å, $b = 13.886$ Å, $c = 14.152$ Å, $\alpha = 104.38°$, $\beta = 101.41°$, $\gamma = 119.29°$. Like other typical $Au_{25}(SR)_{18}$ clusters, $Au_{25}(SC_2H_5)_{18}$ is composed of an inner Au_{13} icosahedral core protected by six (SC_2H_5)−Au−(SC_2H_5)−Au−(SC_2H_5) dimeric staple motifs. The intracluster Au−Au distances from the DFT optimization (Au_{center}−Au_{shell} = 2.85 Å; Au_{shell}−Au_{shell} = 2.99 Å; Au_{shell}−Au_{staple} = 3.29 Å) agree very well with the experiment (Au_{center}−Au_{shell} = 2.79 Å; Au_{shell}−Au_{shell} = 2.94 Å; Au_{shell}−Au_{staple} = 3.18 Å). The intercluster Au−Au distance is about 7% underestimated by DFT (3.82 Å) than the experiment (4.11 Å), likely due to two factors: (i) we fixed the lattice parameters to the experimental values during DFT optimization to maintain the cell shape for the subsequent pressurization simulations; (ii) the intercluster Au−Au interaction is much weaker and therefore sensitive to the intercluster ligand−ligand interactions. We expect that the DFT description of the intercluster Au−Au distances would become more accurate, as the Au−Au interactions are strengthened with the pressure.

Starting from the ground-state structure of $Au_{25}(SC_2H_5)_{18}$, the high-pressure structures were obtained by continuously and uniformly shrinking the volume or lattice constants of $Au_{25}(SC_2H_5)_{18}$: the lattice parameters a, b, and c (Table 1) were scaled by the same factor, such that the crystal symmetry and the lattice ratios of c/a and b/a are kept fixed on compression. After each scaling, the atomic positions in the unit cell were reoptimized with fixed unit cell vectors; after convergence, the pressure was then evaluated by computing the external force on the unit cell. Spin-polarized calculations with an initial ferromagnetic state were performed for the $Au_{25}(SC_2H_5)_{18}$ crystal under different pressures.

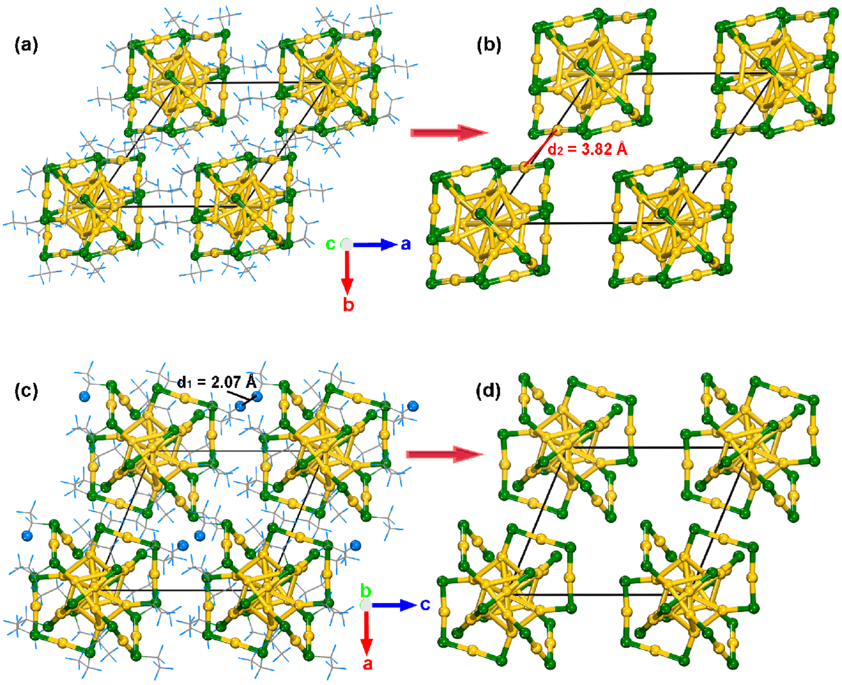

Figure 1. Ambient pressure structure of the crystal phase of $Au_{25}(SC_2H_5)_{18}^0$ cluster (a,c) and the corresponding Au−S framework omitting the ethyl (C_2H_5) groups (b,d), viewed along two different directions: (a,b) are projected along the *c*-axis; (c,d) are projected along the *b*-axis. Color code: Au, orange; S, green; C, gray; H, blue (lines with some highlighted balls). Same color code is used subsequently.

https://doi.org/10.1021/acsnanoscienceau.1c00024
ACS Nanosci. Au 2022, 2, 40−48

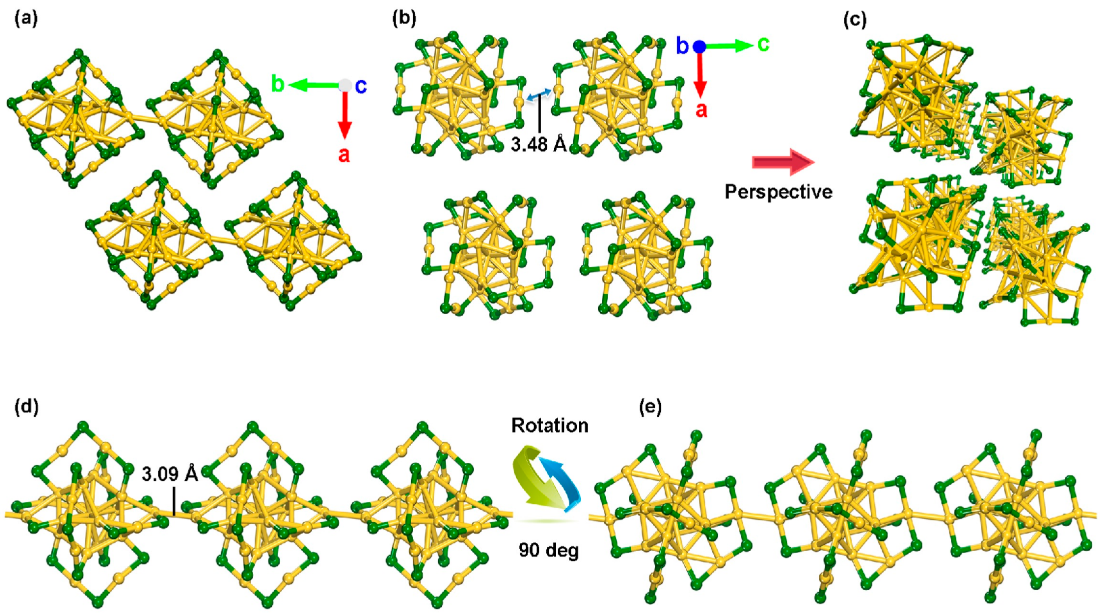

Figure 2. $Au_{25}(SC_2H_5)_{18}$ crystal at 10 GPa (C_2H_5 omitted for clarity): (a) viewed along the *c*-axis; (b) viewed along the *b*-axis; (c) perspective view of four 1D nanowires along the *b*-axis; (d,e) two different side views of the $Au_{25}(SC_2H_5)_{18}$ nanowire and the intercluster Au−Au linkages.

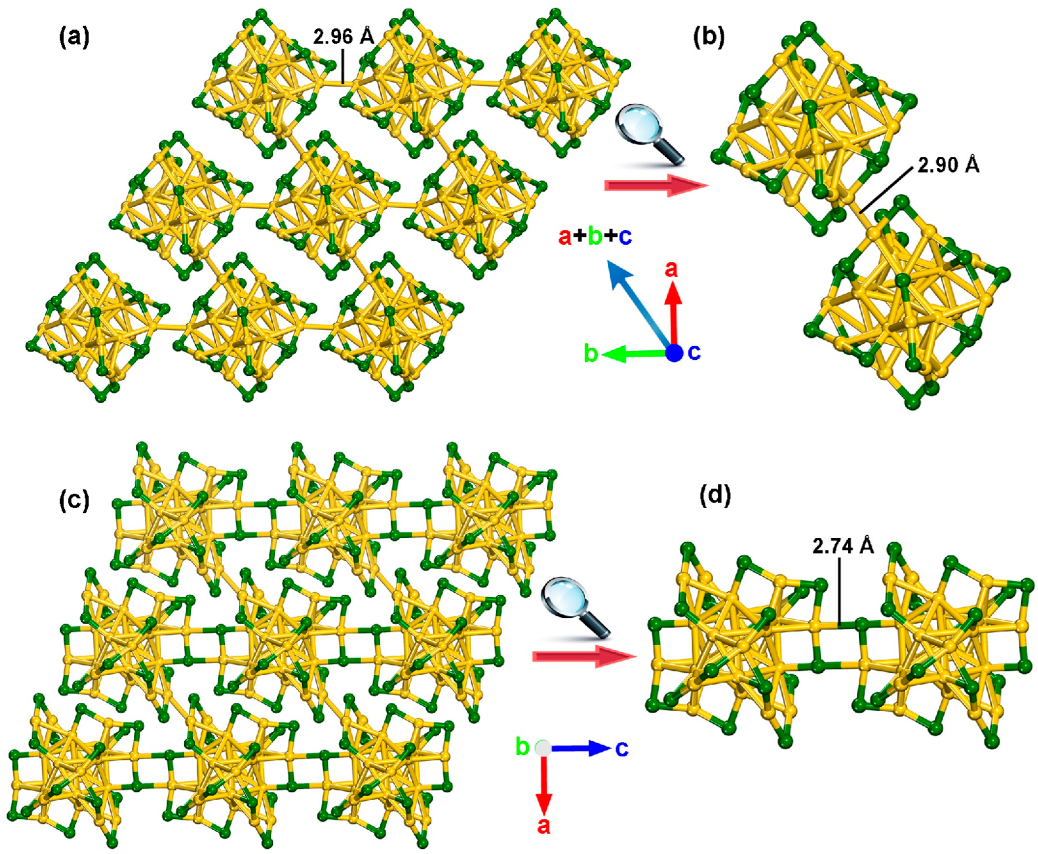

Figure 3. $Au_{25}(SC_2H_5)_{18}$ crystal at 25 GPa (C_2H_5 omitted for clarity): (a) viewed along the *c*-axis; (b) zoom-in on the Au−Au bond formed along the diagonal or **a** + **b** + **c** direction; (c) viewed along the *b*-axis; (d) zoom-in on the interstaple Au−S bonds and rectangle along the *c*-axis.

RESULTS AND DISCUSSION

Crystal Structure of $Au_{25}(SC_2H_5)_{18}{}^0$ at Ambient Pressure

As shown in Figure 1, the clusters in the crystal are weakly interacting with each other via vdW interactions among ethyl groups (blue lines in Figure 1a,c) of the staple motifs: the shortest intermolecular H⋯H distance between ethyl groups is 2.07 Å (d_1 in Figure 1c). The shortest intercluster Au⋯Au distance between two staple motifs is 3.82 Å (d_2 in Figure 1b).

To define a criterion or distance cutoff for chemical bonding, we use the average of the covalent and vdW radii of an atom (Table 2): If the distance between two atoms is shorter than

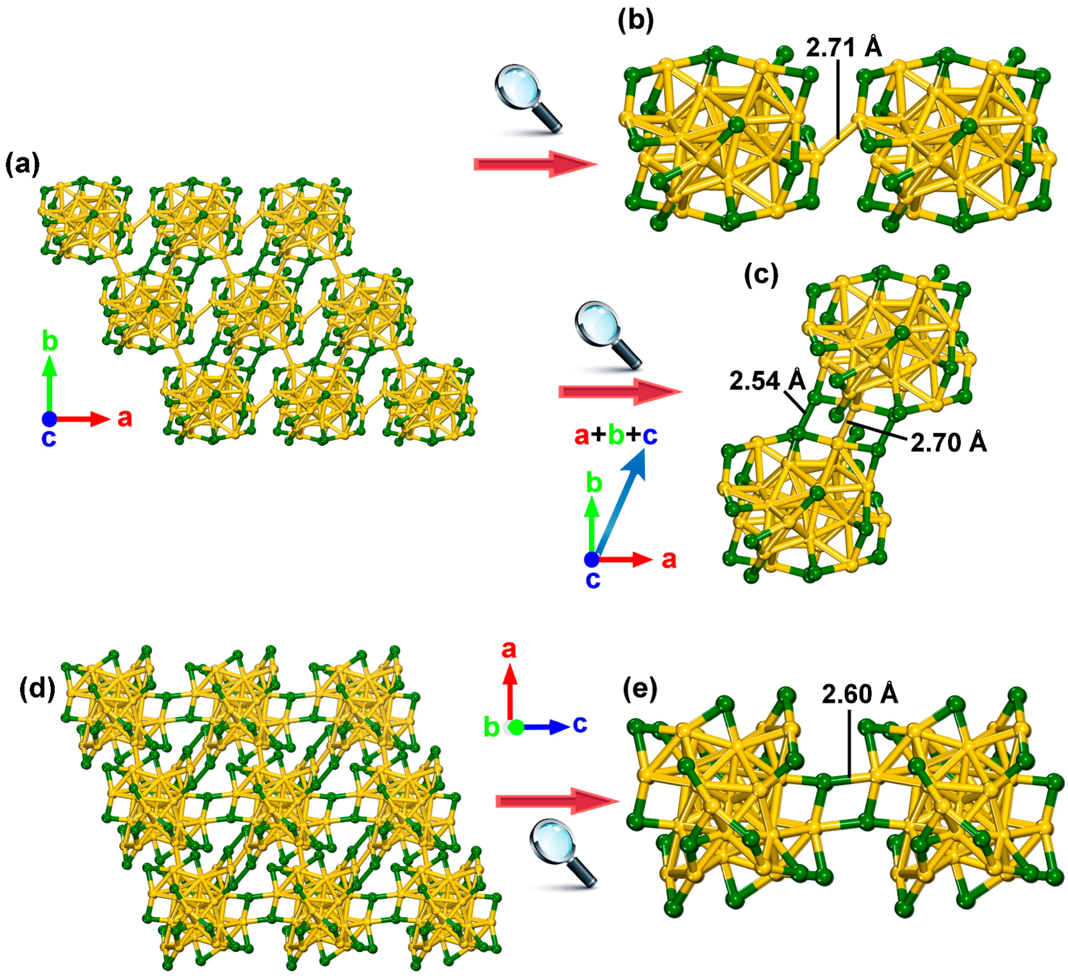

Figure 4. $Au_{25}(SC_2H_5)_{18}$ crystal at 50 GPa (C_2H_5 omitted for clarity): (a) viewed along the *c*-axis; (b) zoom-in view of the intercluster Au−Au bond formed along the *a*-axis; (c) zoom-in view of the intercluster Au−Au and S−S bonds along the diagonal (***a*** + ***b*** + **c**); (d) viewed along the *b*-axis; (e) zoom-in view of the deformation of the intercluster −Au−S−Au−S− ring along the *c*-axis.

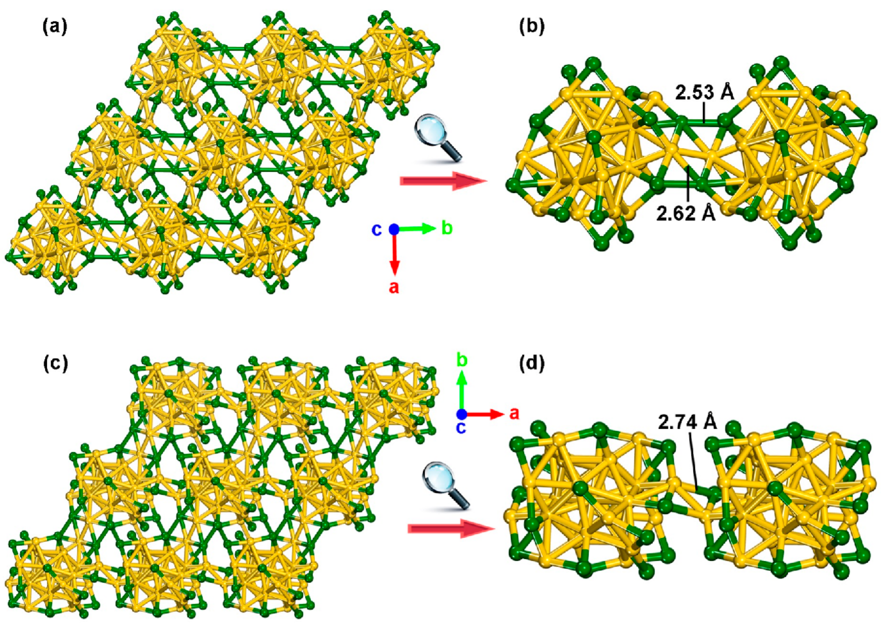

Figure 5. $Au_{25}(SC_2H_5)_{18}$ crystal at 80 GPa (C_2H_5 omitted for clarity): (a) viewed along the *c*-axis; (b) zoom-in view of the intercluster Au−S and S−S bonds along the *b*-axis; (c) viewed along the *c*-axis in a different perspective; (d) zoom-in view of the intercluster Au−S bonds along the *a*-axis.

https://doi.org/10.1021/acsnanoscienceau.1c00024
ACS Nanosci. Au 2022, 2, 40−48

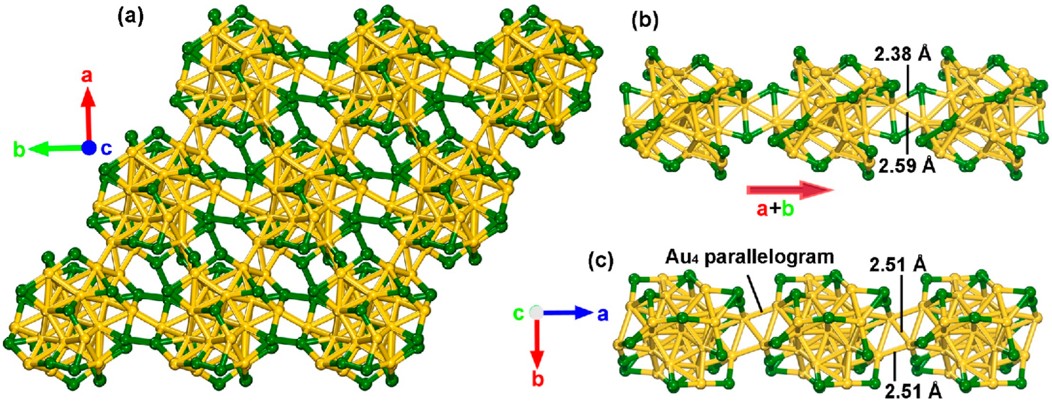

Figure 6. $Au_{25}(SC_2H_5)_{18}$ crystal at 110 GPa (C_2H_5 omitted for clarity): (a) viewed along the *c*-axis; (b) zoom-in view of the intercluster Au−S and Au−Au bonds along *a* + *b* direction; (c) zoom-in view of the intercluster Au_4 parallelogram along the *a*-axis.

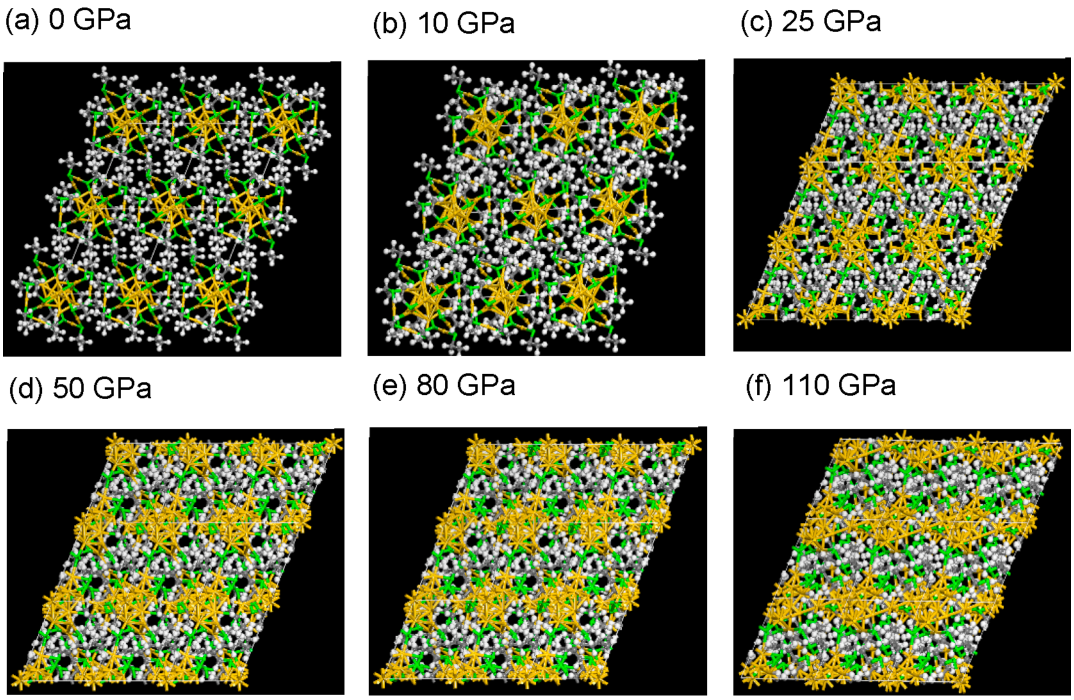

Figure 7. Packed structure of the $Au_{25}(SC_2H_5)_{18}$ crystal at various pressures showing also the C_2H_5 groups.

the sum of their average radii, a chemical bond is formed or there is a chemical interaction between the two atoms. By our definition, there is no intercluster chemical interaction at ambient pressure here, since the shortest Au⋯Au and H⋯H distances between neighboring $Au_{25}(SC_2H_5)_{18}$ clusters are much larger than the bond-length cutoff of the Au−Au (3.10 Å) and H−H (1.58 Å) chemical interactions, respectively.

According to the superatom complex theory,[44] the isolated neutral $Au_{25}(SC_2H_5)_{18}$ cluster has seven free electrons, which occupy the superatomic orbitals as $(1S)^2(1P)^5$, thereby possessing an unpaired valence electron at the HOMO. This is consistent with our calculations: we found that the unit cell of the $Au_{25}(SC_2H_5)_{18}$ crystal, which contains just one formula unit of the cluster, has a net magnetic moment of 1 μ_B.

At 10 GPa

Figure 2 shows the Au−S framework of the compressed $Au_{25}(SC_2H_5)_{18}{}^0$ crystal structure at an external pressure of 10 GPa. One can clearly see that the intercluster distance decreases, leading to the formation of an intercluster Au−Au bond of 3.09 Å along the *b*-axis (Figure 2a,d) between the staple motifs, which joins the clusters to form a one-dimensional (1D) nanowire along the *b*-axis (Figure 2c−e). The closest Au⋯Au contact between the 1D nanowires is about 3.48 Å along the *c*-axis (Figure 2b). Interestingly, we found that the magnetic moment of the $Au_{25}(SC_2H_5)_{18}$ crystal disappeared (μ_B = 0) at 10 GPa. This can be understood in that the unpaired electrons in $Au_{25}(SC_2H_5)_{18}$ clusters are now paired up after forming the intercluster Au−Au bonds, leading to the vanishing magnetic moment. In fact, the nanowire-like 1D polymeric chain of $Au_{25}(SR)_{18}{}^0$ has been previously reported in the solid state of another neutral $Au_{25}(SR)_{18}{}^0$ nanocluster capped by *n*-butanethiolate (SBu) ligands.[45]

At 25 GPa

As the pressure further increases to 25 GPa, the intercluster Au−Au bond between the staple motifs along the *b*-axis is further decreased to 2.96 Å (Figure 3a). In addition, we observed a newly formed intercluster Au−Au bond of 2.90 Å (Figure 3b) along the diagonal direction of the unit cell

https://doi.org/10.1021/acsnanoscienceau.1c00024
ACS Nanosci. Au 2022, 2, 40−48

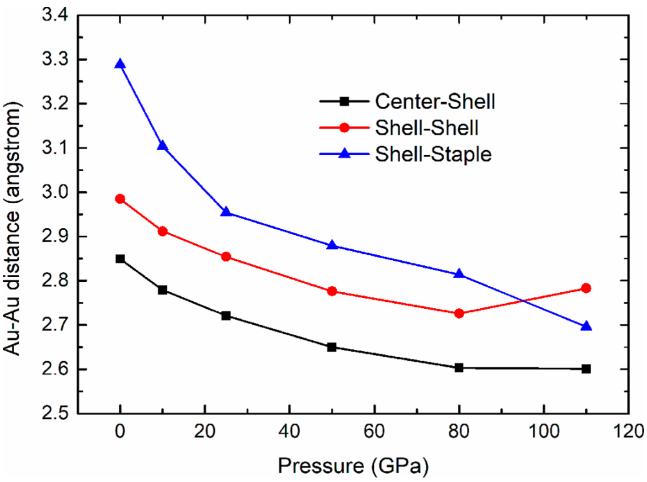

Figure 8. Variation of intracluster Au−Au distances of $Au_{25}(SC_2H_5)_{18}$ with pressure: Center-Shell, average distance from the central Au to the 12 Au atoms of the the icosahedral shell; Shell-Shell, average nearest-neighbor distance among the 12 Au atoms of the icosahedral shell; Shell-Staple, average nearest-neighbor distance between staple Au atoms and the icosahedral-shell Au atoms.

(namely, ***a*** + *b* + *c* or [111] direction) and intercluster Au−S bonds of 2.74 Å along the *c*-axis (Figure 3c,d). In fact, the latter further forms a rectangle-shaped, four-membered ring between intercluster staple motifs. This indicates that from 10 to 25 GPa, the crystalline phase of $Au_{25}(SC_2H_5)_{18}$ transitions from the stacked 1D nanowires to a 3D interconnected network. Similar to the case at 10 GPa, the compressed $Au_{25}(SC_2H_5)_{18}$ at 25 GPa has no unpaired electron.

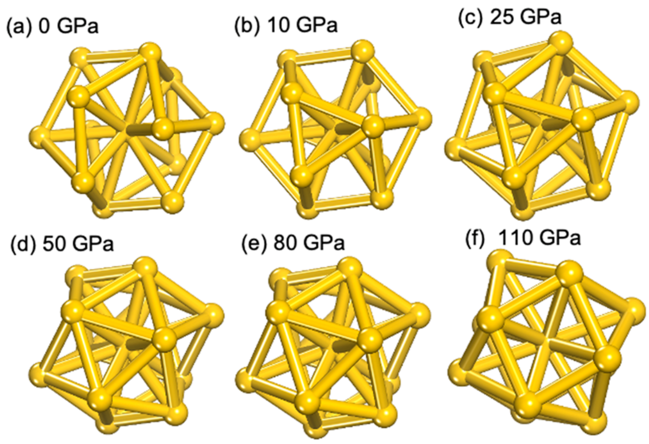

Figure 10. Structural change of the Au_{13} core with pressure. Note that 3.1 Å is used as the cutoff for drawing a bond between two Au atoms.

At 50 GPa

The 3D framework of the $Au_{25}(SC_2H_5)_{18}$ solid becomes strengthened when the pressure increases to 50 GPa (Figure 4). In addition to the much shortened intercluster Au−Au bond (2.60 Å) along the *b*-axis (Figure 4a) and Au−S bonds (2.60 Å) along the *c*-axis (Figure 4e), the $Au_{25}(SC_2H_5)_{18}$ lattice additionally forms a new intercluster Au−Au bond (2.71 Å) along the *a*-axis (Figure 4b). More interestingly, two new S−S bonds (2.54 Å) are formed, flanking the Au−Au bond (2.70 Å) along the diagonal direction (Figure 4c); put in another way, two parallel linear S−Au−S groups from the two staple motifs fuse together into a three-rung ladder. One also sees that the −Au−S−Au−S− rectangle along the *c*-axis at 25 GPa now deforms to a parallelogram at 50 GPa (Figure 4e).

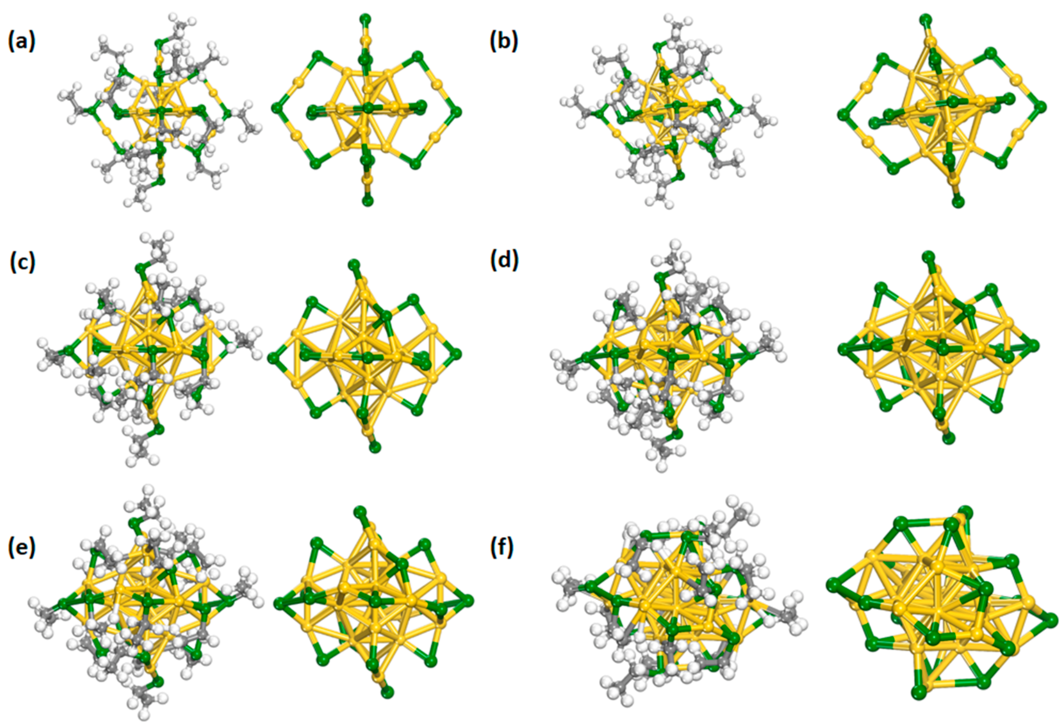

Figure 9. Structure of the $Au_{25}(SC_2H_5)_{18}$ cluster (left) and its Au−S framework (right) in the crystal at various pressures: (a) ambient; (b) 10 GPa; (c) 25 GPa; (d) 50 GPa; (e) 80 GPa; (f) 110 GPa.

https://doi.org/10.1021/acsnanoscienceau.1c00024
ACS Nanosci. Au 2022, 2, 40−48

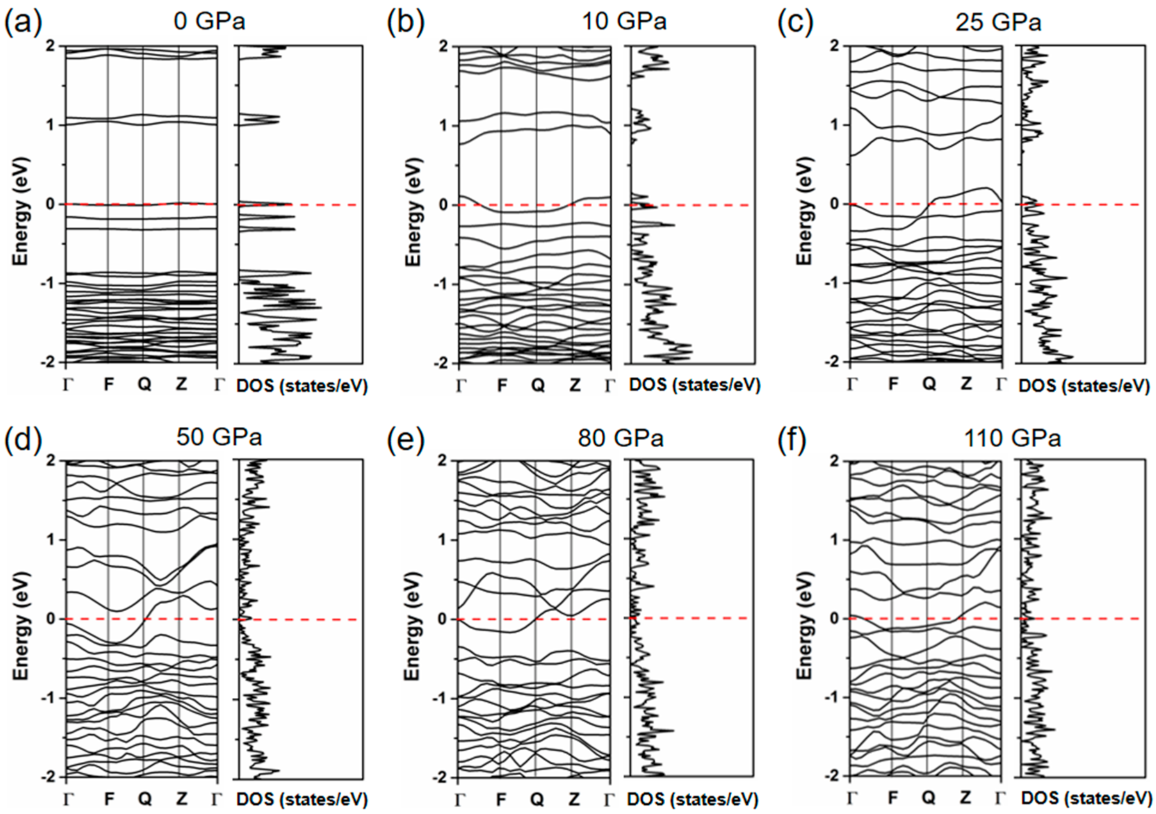

Figure 11. Band structure and density of states of $Au_{25}(SC_2H_5)_{18}$ crystal at various pressures: (a) ambient; (b) 10 GPa; (c) 25 GPa; (d) 50 GPa; (e) 80 GPa; (f) 110 GPa. The Fermi level is set as zero and denoted by the dashed red line.

At 80 GPa

As the pressure goes up to 80 GPa, the intercluster linkages are greatly enhanced (Figure 5). Not only are the three-rung ladder connection along the diagonal and the parallelogram connection along the *c*-axis well preserved, but a new type of three-rung ladder-like linkage (Figure 5a,b) and a new parallelogram connection (Figure 5c,d) are also formed along the *b*-axis and the *a*-axis, respectively.

At 110 GPa

As the pressure increases to 110 GPa, one sees the formation of more complicated intercluster linkages, accompanied by a great deformation of the Au_{13} core, in addition to the slightly changed three-rung ladder-like bond pattern (Figure 6a) and parallelogram or diamond-shaped connection (Figure 6b). Particularly, a new type of intercluster edge-sharing Au_4 parallelogram emerges along the *a*-axis (Figure 6c).

We note that in the compressed $Au_{25}(SC_2H_5)_{18}$ crystal, the $-C_2H_5$ ligands are interacting in shorter distances (Figure 7). According to our structural analysis, the shortest intercluster H−H distances are 1.620 Å (10 GPa), 1.633 Å (25 GPa), 1.475 Å (50 GPa), 1.460 Å (80 GPa), and 1.326 Å (110 GPa); the shortest intercluster C−H distances are 2.368 Å (10 GPa), 2.175 Å (25 GPa), 2.168 Å (50 GPa), 2.122 Å (80 GPa), and 2.012 Å (110 GPa). Based on the cutoffs of 1.58 Å for H−H and 2.03 Å for C−H (Table 2), the intercluster H−H interactions are mainly physical or of the dispersion type up to 25 GPa (Figure 7a−c) but become chemical at 50 GPa or higher (Figure 7d−f), while the intercluster C−H chemical interaction can be found only at 110 GPa (Figure 7f). In other words, $-C_2H_5$ ligands are interacting with each other mainly via H−H chemical bonding at higher pressures.

Intracluster Change with Pressure

In addition to the interesting intercluster bonding over a broad range of pressures, it is also of great interest to examine the structural changes to the $Au_{25}(SC_2H_5)_{18}$ cluster itself inside the crystal during compression. Figure 8 presents the variation of key intracluster Au−Au bond distances with pressure that shows an expected decreasing trend. Examining the overall cluster shape, one can see that the structural integrity of the $Au_{25}(SC_2H_5)_{18}$ cluster (Figure 9a) is well preserved at 10 GPa (Figure 9b), while more Au−Au bonds are formed between staple Au atoms and the icosahedral Au atoms. Starting at 25 GPa (Figure 9c), the S−Au−S−Au-S staple motifs become distorted, intrastaple Au−Au bonds are formed, and some terminal S atoms of one staple become bonded with Au in a nearby staple. At 50 GPa, the staples become more twisted and S−S bonds begin to form between the nearest staples (Figure 9d); in addition, there is bonding between H on C_2H_5 and the icosahedral Au atoms (six Au−H bonds are formed with Au−H distance of ∼2.0 Å). At 80 GPa (Figure 9e) and 110 GPa (Figure 9f), one sees formation of more S−S bonds, Au−H bonds, and Au−S bonds.

The structural evolution of the Au_{13} core with pressure is shown in Figure 10. The icosahedral Au_{13} core in the ambient $Au_{25}(SC_2H_5)_{18}$ crystal has an approximate I_h symmetry. With the pressure increasing, the Au_{13} core becomes compressed but still maintains the I_h symmetry at 10 and 25 GPa (Figure 10b,c). However, the Au_{13} core becomes significantly more distorted and squashed starting at 50 GPa (Figure 10d), and a distinct transition takes place from 80 (Figure 10e) to 110 Ga where the Au_{13} core switches to an O_h-like symmetry (Figure 10f).

https://doi.org/10.1021/acsnanoscienceau.1c00024
ACS Nanosci. Au 2022, 2, 40−48

Electronic Structure Change with Pressure

The electronic band structures and density of states for the ambient state and the compressed $Au_{25}(SC_2H_5)_{18}$ structures were also explored, which show a strong structure dependence. One can see that the $Au_{25}(SC_2H_5)_{18}$ crystal at ambient pressure has flat and discrete energy bands, characteristic of a typical molecular crystal (Figure 11a). Starting at the pressure of 10 GPa (Figure 11b), one sees clear band dispersion, and the band at the Fermi level becomes partially occupied, indicating a metallic character. When the pressure further increases (Figure 11c−f), the conduction band above the Fermi level gradually shifts downward while the valence band below Fermi level shifts upward. This leads to the broadening and delocalization of the energy states, and the bands also become more dispersed. Moreover, all of the compressed $Au_{25}(SC_2H_5)_{18}$ crystals (10 ∼ 110 GPa) are nonmagnetic.

CONCLUSIONS

In summary, we explored systematically the structural and electronic properties of the $Au_{25}(SC_2H_5)_{18}$ superatomic cluster under pressure (up to 110 GPa). Our DFT computations discovered that under compression the $Au_{25}(SC_2H_5)_{18}$ cluster changes from a molecular crystal to an interconnected solid crystal, due to the formation of intercluster Au−Au, Au−S, S−S, and H−H bonds. We also observed the formation of intracluster Au−Au, Au−S, S−S, and Au−H bonds. At ambient pressure, the $Au_{25}(SC_2H_5)_{18}$ cluster has an unpaired valence electron; upon compression, the cluster interacts closely with each other to pair the valence electron and the magnetic moment vanishes. All of the compressed clusters are predicted to be metallic. Our DFT findings represent an important step toward understanding the high-pressure behavior of superatomic gold nanoclusters. We hope that this work will stimulate more experiments in the future on the structure, bonding, and conductivity measurements of atomically precise metal nanoclusters under high pressures.

ASSOCIATED CONTENT

Supporting Information

The Supporting Information is available free of charge at https://pubs.acs.org/doi/10.1021/acsnanoscienceau.1c00024.

Coordinates of the optimized atomic positions in the $Au_{25}(SC_2H_5)_{18}$ crystal at various pressures (PDF)

AUTHOR INFORMATION

Corresponding Author

De-en Jiang − *Department of Chemistry, University of California, Riverside, California 92521, United States;* orcid.org/0000-0001-5167-0731; Email: djiang@ucr.edu

Authors

Qing Tang − *School of Chemistry and Chemical Engineering, Chongqing Key Laboratory of Theoretical and Computational Chemistry, Chongqing University, Chongqing 401331, China;* orcid.org/0000-0003-0805-7506

Fuhua Li − *School of Chemistry and Chemical Engineering, Chongqing Key Laboratory of Theoretical and Computational Chemistry, Chongqing University, Chongqing 401331, China*

Complete contact information is available at: https://pubs.acs.org/10.1021/acsnanoscienceau.1c00024

Notes

The authors declare no competing financial interest.

ACKNOWLEDGMENTS

This work was sponsored by the University of California Riverside. This research used resources of the National Energy Research Scientific Computing Center, a DOE Office of Science User Facility supported by the Office of Science of the U.S. Department of Energy under Contract No. DE-AC02-05CH11231.

REFERENCES

(1) Duan, D. F.; Liu, Y. X.; Tian, F. B.; Li, D.; Huang, X. L.; Zhao, Z. L.; Yu, H. Y.; Liu, B. B.; Tian, W. J.; Cui, T. Pressure-induced metallization of dense $(H_2S)_2H_2$ with high-Tc superconductivity. *Sci. Rep.* **2015**, *4*, 6968.

(2) Drozdov, A. P.; Kong, P. P.; Minkov, V. S.; Besedin, S. P.; Kuzovnikov, M. A.; Mozaffari, S.; Balicas, L.; Balakirev, F. F.; Graf, D. E.; Prakapenka, V. B.; Greenberg, E.; Knyazev, D. A.; Tkacz, M.; Eremets, M. I. Superconductivity at 250 K in lanthanum hydride under high pressures. *Nature* **2019**, *569*, 528−531.

(3) Matsuoka, T.; Shimizu, K. Direct observation of a pressure-induced metal-to-semiconductor transition in lithium. *Nature* **2009**, *458*, 186−189.

(4) Babaev, E.; Sudbo, A.; Ashcroft, N. W. A superconductor to superfluid phase transition in liquid metallic hydrogen. *Nature* **2004**, *431*, 666−668.

(5) Pickard, C. J.; Needs, R. J. High-pressure phases of silane. *Phys. Rev. Lett.* **2006**, *97*, No. 045504.

(6) Drozdov, A. P.; Eremets, M. I.; Troyan, I. A.; Ksenofontov, V.; Shylin, S. I. Conventional superconductivity at 203 K at high pressures in the sulfur hydride system. *Nature* **2015**, *525*, 73−76.

(7) Miao, M. S.; Hoffmann, R. High Pressure Electrides: A Predictive Chemical and Physical Theory. *Acc. Chem. Res.* **2014**, *47*, 1311−1317.

(8) Naumov, I. I.; Hemley, R. J.; Hoffmann, R.; Ashcroft, N. W. Chemical bonding in hydrogen and lithium under pressure. *J. Chem. Phys.* **2015**, *143*, No. 064702.

(9) Miao, M. S.; Hoffmann, R.; Botana, J.; Naumov, I. I.; Hemley, R. J. Quasimolecules in Compressed Lithium. *Angew. Chem., Int. Ed.* **2017**, *56*, 972−975.

(10) Prasad, D.; Ashcroft, N. W.; Hoffmann, R. Evolving Structural Diversity and Metallicity in Compressed Lithium Azide. *J. Phys. Chem. C* **2013**, *117*, 20838−20846.

(11) Behler, J.; Martonak, R.; Donadio, D.; Parrinello, M. Metadynamics simulations of the high-pressure phases of silicon employing a high-dimensional neural network potential. *Phys. Rev. Lett.* **2008**, *100*, 185501.

(12) AlKaabi, K.; Prasad, D.; Kroll, P.; Ashcroft, N. W.; Hoffmann, R. Silicon Monoxide at 1 atm and Elevated Pressures: Crystalline or Amorphous? *J. Am. Chem. Soc.* **2014**, *136*, 3410−3423.

(13) Kuwayama, Y.; Hirose, K.; Sata, N.; Ohishi, Y. The pyrite-type high-pressure form of silica. *Science* **2005**, *309*, 923−925.

(14) Wang, Y. C.; Ma, Y. M. Perspective: Crystal structure prediction at high pressures. *J. Chem. Phys.* **2014**, *140*, No. 040901.

(15) Zhang, L. J.; Wang, Y. C.; Lv, J.; Ma, Y. M. Materials discovery at high pressures. *Nat. Rev. Mater.* **2017**, *2*, 17005.

(16) Jin, R.; Zeng, C.; Zhou, M.; Chen, Y. Atomically Precise Colloidal Metal Nanoclusters and Nanoparticles: Fundamentals and Opportunities. *Chem. Rev.* **2016**, *116*, 10346−10413.

(17) Chakraborty, I.; Pradeep, T. Atomically Precise Clusters of Noble Metals: Emerging Link between Atoms and Nanoparticles. *Chem. Rev.* **2017**, *117*, 8208−8271.

(18) Du, Y. X.; Sheng, H. T.; Astruc, D.; Zhu, M. Z. Atomically Precise Noble Metal Nanoclusters as Efficient Catalysts: A Bridge between Structure and Properties. *Chem. Rev.* **2020**, *120*, 526−622.

(19) Kang, X.; Li, Y. W.; Zhu, M. Z.; Jin, R. C. Atomically precise alloy nanoclusters: syntheses, structures, and properties. *Chem. Soc. Rev.* **2020**, *49*, 6443−6514.

(20) Li, G.; Jin, R. C. Atomically Precise Gold Nanoclusters as New Model Catalysts. *Acc. Chem. Res.* **2013**, *46*, 1749−1758.

(21) Tang, Q.; Hu, G. X.; Fung, V.; Jiang, D. E. Insights into Interfaces, Stability, Electronic Properties, and Catalytic Activities of Atomically Precise Metal Nanoclusters from First Principles. *Acc. Chem. Res.* **2018**, *51*, 2793−2802.

(22) Chai, O. J. H.; Liu, Z.; Chen, T.; Xie, J. Engineering ultrasmall metal nanoclusters for photocatalytic and electrocatalytic applications. *Nanoscale* **2019**, *11*, 20437−20448.

(23) Jin, R. C.; Li, G.; Sharma, S.; Li, Y. W.; Du, X. S. Toward Active-Site Tailoring in Heterogeneous Catalysis by Atomically Precise Metal Nanoclusters with Crystallographic Structures. *Chem. Rev.* **2021**, *121*, 567−648.

(24) Tao, Y.; Li, M. Q.; Ren, J. S.; Qu, X. G. Metal nanoclusters: novel probes for diagnostic and therapeutic applications. *Chem. Soc. Rev.* **2015**, *44*, 8636−8663.

(25) Loynachan, C. N.; Soleimany, A. P.; Dudani, J. S.; Lin, Y. Y.; Najer, A.; Bekdemir, A.; Chen, Q.; Bhatia, S. N.; Stevens, M. M. Renal clearable catalytic gold nanoclusters for in vivo disease monitoring. *Nat. Nanotechnol.* **2019**, *14*, 883−890.

(26) Srinivasulu, Y. G.; Yao, Q. F.; Goswami, N.; Xie, J. P. Interfacial engineering of gold nanoclusters for biomedical applications. *Mater. Horiz.* **2020**, *7*, 2596−2618.

(27) Zheng, Y. K.; Wu, J. B.; Jiang, H.; Wang, X. M. Gold nanoclusters for theranostic applications. *Coord. Chem. Rev.* **2021**, *431*, 213689.

(28) Goswami, N.; Lin, F. X.; Liu, Y. B.; Leong, D. T.; Xie, J. P. Highly Luminescent Thiolated Gold Nanoclusters Impregnated in Nanogel. *Chem. Mater.* **2016**, *28*, 4009−4016.

(29) Xu, M. M.; Jia, T. T.; Li, B. J.; Ma, W.; Chen, X. Y.; Zhao, X. L.; Zang, S. Q. Tuning the properties of atomically precise gold nanoclusters for biolabeling and drug delivery. *Chem. Commun.* **2020**, *56*, 8766−8769.

(30) Li, Q.; Zhou, M.; So, W. Y.; Huang, J. C.; Li, M. X.; Kauffman, D. R.; Cotlet, M.; Higaki, T.; Peteanu, L. A.; Shao, Z. Z.; Jin, R. A Mono-cuboctahedral Series of Gold Nanoclusters: Photoluminescence Origin, Large Enhancement, Wide Tunability, and Structure-Property Correlation. *J. Am. Chem. Soc.* **2019**, *141*, 5314−5325.

(31) Dong, J. W.; Gan, Z. B.; Gu, W. M.; You, Q.; Zhao, Y.; Zha, J.; Li, J.; Deng, H. T.; Yan, N.; Wu, Z. K. Synthesizing Photoluminescent $Au_{28}(SCH_2Ph\text{-}^tBu)_{22}$ Nanoclusters with Structural Features by Using A Combined Method. *Angew. Chem.* **2021**, *133*, 18076−18080.

(32) Malola, S.; Lehtovaara, L.; Enkovaara, J.; Hakkinen, H. Birth of the Localized Surface Plasmon Resonance in Mono layer-Protected Gold Nanoclusters. *ACS Nano* **2013**, *7*, 10263−10270.

(33) Gieseking, R. L. M.; Ashwell, A. P.; Ratner, M. A.; Schatz, G. C. Analytical Approaches To Identify Plasmon-like Excited States in Bare and Ligand-Protected Metal Nanoclusters. *J. Phys. Chem. C* **2020**, *124*, 3260−3269.

(34) Reato, M.; Dainese, T.; Antonello, S.; Maran, F. Electron Transfer in Films of Atomically Precise Gold Nanoclusters. *Chem. Mater.* **2021**, *33*, 4177−4187.

(35) Yoon, B.; Luedtke, W. D.; Barnett, R. N.; Gao, J. P.; Desireddy, A.; Conn, B. E.; Bigioni, T.; Landman, U. Hydrogen-bonded structure and mechanical chiral response of a silver nanoparticle superlattice. *Nat. Mater.* **2014**, *13*, 807−811.

(36) Li, Q.; Mosquera, M. A.; Jones, L. O.; Parakh, A.; Chai, J. S.; Jin, R. C.; Schatz, G. C.; Gu, X. W. Pressure-Induced Optical Transitions in Metal Nanoclusters. *ACS Nano* **2020**, *14*, 11888−11896.

(37) Sun, Q. Q.; Li, Q.; Li, H. Y.; Zhang, M. M.; Sun, M. E.; Li, S.; Quan, Z. W.; Zang, S. Q. Thermochromism and piezochromism of an atomically precise high-nuclearity silver sulfide nanocluster. *Chem. Commun.* **2021**, *57*, 2372−2375.

(38) Kang, X.; Chong, H. B.; Zhu, M. Z. $Au_{25}(SR)_{18}$: the captain of the great nanocluster ship. *Nanoscale* **2018**, *10*, 10758−10834.

(39) Dainese, T.; Antonello, S.; Gascon, J. A.; Pan, F. F.; Perera, N. V.; Ruzzi, M.; Venzo, A.; Zoleo, A.; Rissanen, K.; Maran, F. $Au_{25}(SEt)_{18}$, a Nearly Naked Thiolate-Protected Au_{25} Cluster: Structural Analysis by Single Crystal X-ray Crystallography and Electron Nuclear Double Resonance. *ACS Nano* **2014**, *8*, 3904−3912.

(40) Kresse, G.; Furthmuller, J. Efficient Iterative Schemes for ab Initio Total-Energy Calculations Using a Plane-Wave Basis Set. *Phys. Rev. B: Condens. Matter Mater. Phys.* **1996**, *54*, 11169−11186.

(41) Blochl, P. E. Projector Augmented-Wave Method. *Phys. Rev. B: Condens. Matter Mater. Phys.* **1994**, *50*, 17953−17979.

(42) Perdew, J. P.; Burke, K.; Ernzerhof, M. Generalized gradient approximation made simple. *Phys. Rev. Lett.* **1996**, *77*, 3865−3868.

(43) Grimme, S.; Antony, J.; Ehrlich, S.; Krieg, H. A Consistent and Accurate ab Initio Parametrization of Density Functional Dispersion Correction (DFT-D) for the 94 Elements H-Pu. *J. Chem. Phys.* **2010**, *132*, 154104.

(44) Walter, M.; Akola, J.; Lopez-Acevedo, O.; Jadzinsky, P. D.; Calero, G.; Ackerson, C. J.; Whetten, R. L.; Gronbeck, H.; Hakkinen, H. A unified view of ligand-protected gold clusters as superatom complexes. *Proc. Natl. Acad. Sci. U. S. A.* **2008**, *105*, 9157−9162.

(45) De Nardi, M.; Antonello, S.; Jiang, D. E.; Pan, F. F.; Rissanen, K.; Ruzzi, M.; Venzo, A.; Zoleo, A.; Maran, F. Gold Nanowired: A Linear $(Au_{25})_n$ Polymer from Au_{25} Molecular Clusters. *ACS Nano* **2014**, *8*, 8505−8512.